Power Electronic Systems
Laboratory

© 2014 IEEE

Proceedings of the 40th Annual Conference of the IEEE Industrial Electronics Society (IECON 2014), Dallas, Texas, USA, October 29-November 1, 2014

Weight Optimization of a Machine for Airborne Wind Turbines

C. Gammeter,
Y. Drapela,
A. Tüysüz,
J. W. Kolar

This material is published in order to provide access to research results of the Power Electronic Systems Laboratory / D-ITET / ETH Zurich. Internal or personal use of this material is permitted. However, permission to reprint/republish this material for advertising or promotional purposes or for creating new collective works for resale or redistribution must be obtained from the copyright holder. By choosing to view this document, you agree to all provisions of the copyright laws protecting it.

Eidgenössische Technische Hochschule Zürich
Swiss Federal Institute of Technology Zurich

Weight Optimization of a Machine for Airborne Wind Turbines

Christoph Gammeter, Yannick Drapela, Arda Tüysüz and Johann W. Kolar
Power Electronic Systems Laboratory
Swiss Institute of Technology,
Physikstrasse 3
8092 Zurich, Switzerland

***Abstract*—This paper details the weight optimization of the electrical machine required for an Airborne Wind Turbine (AWT) system. Presented investigations include the analysis of the power-to-weight ratio versus efficiency limits, γ-η Pareto fronts, of radial and axial flux machine topologies, by making use of analytical models, describing the electromagnetic and thermal behaviour. A direct search method is employed rather than a cost function minimization algorithm, as the analytical models allow the evaluation of the whole design space in a computationally efficient manner. The results reveal that the best performance in this case is achieved with a radial flux machine with an internal rotor where the magnets are arranged in a Halbach configuration. Including the weight of electromagnetically inactive parts, such as bearings, shaft and housing, a power-to-weight ratio of $\gamma \approx 6.2\,\mathrm{kW/kg}$ ($2.8\,\mathrm{kW/lb}$), at an efficiency of $\eta \approx 96\,\%$, and a rated speed of $3200\,\mathrm{r/min}$ is achieved.**

I. Introduction

Increasing consumption of electric energy, environmental issues, and limited availability of fossil fuels have led to a multitude of developments related to the generation of electricity from renewable energy sources. One innovative system in this context is the Airborne Wind Turbine (AWT) detailed in [1], which generates electricity from high altitude winds. High altitude winds are known to be more stable and faster than winds close to ground-level, thus, enable a more reliable and effective generation of electric energy [1]. Furthermore, the AWT is essentially a flying wing with a significantly lower construction effort of the power generation system compared to conventional wind turbine concepts. A tether, i.e. a long fiber and cable combination ($\approx 1\,\mathrm{km}$ long), ties the AWT to the ground and, additionally, provides the electrical link to the ground station [1]. The greatest challenge with respect to the realization of the electric system of the AWT is to achieve a light-weight cable and light-weight generators and power converters. The considered AWT system is rated for a maximum output power of $100\,\mathrm{kW}$.

Related investigations detailed in [1] reveal that a low-weight realization of the AWT makes a dc–dc converter necessary, which boosts the dc bus voltage, V_1, on-board the AWT ($650\,\mathrm{V} < V_1 < 750\,\mathrm{V}$) to a high cable voltage of up to $8\,\mathrm{kV}$, cf. Fig. 1. Furthermore, the dc–dc converter needs to allow for bi-directional energy transfer in order to enable the start-up of the AWT.

Fig. 1 depicts the electrical system for the AWT proposed in [1]; four bi-directional dc–dc converters are linking eight generators with voltage source rectifiers to a tether and a bi–directional dc–ac converter connects the tether to the three-phase grid on the ground. The converter topology for the dc–dc converter is detailed in [1]–[3]. The AWT uses the electrical

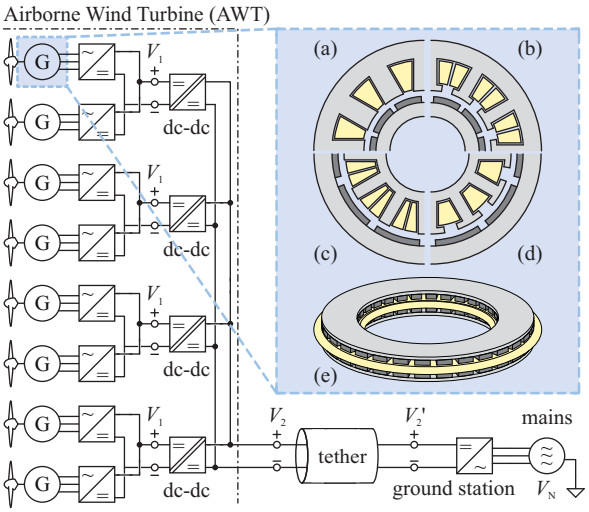

Fig. 1. Electrical system of the Airborne Wind Turbine (AWT); four bi-directional dc–dc converters are linking eight generators with voltage source rectifiers, port voltage V_1, to a tether ($\approx 1\,\mathrm{km}$), port voltage V_2. The ground station, i.e. bi-directional dc–ac converter, connects the tether to the three-phase grid. (a)–(d) Geometrical models of the considered radial flux machines (RFM), (e) geometrical model of the considered double-rotor axial flux machines (AFM).

machines in generator operation during cross wind flight and in motor operation for launching and landing sequences. The optimization of the electrical machines with respect to minimum weight is of particular interest, as they contribute about half of the total electrical system weight installed on the AWT [1].

Ragot [4]–[6] optimized a brushless direct current (BLDC) machine with internal rotor for a solar airplane application. Ragot's system description has 110 parameters linked by 70 equations and is optimized using a commercial software, which provides a solution minimizing an objective function while satisfying a set of constraints. This approach, however, relies on an objective function, which can only be properly defined with knowledge of the sensitivity of competing objectives, e.g. $\mathrm{d}\eta/\mathrm{d}\gamma$, which may not be known a priori. Van der Geest [7] recognizes the importance of proper machine topology selection at the beginning of a project, i.e. for each set of specifications, and gives a procedure to compare different machines based on numerical two dimensional (2D) finite element analysis (FEA) guided by particle swarm optimization (PSO). The loss of insight originating from the objective function required for PSO is circumvented by multi-target

optimization enabling the results to be presented as Pareto optimal fronts. Van der Geest then applies his method in [8] to select a machine for an aerospace starter/generator, by comparing seven surface mounted permanent magnet (SPM) machines and two switched reluctance machines (SRM). Van der Geest's approach however relies on FEA which is computationally expensive and therefore limited to 2D analysis. Although sensitivity analysis of competing objectives may be achieved, there is limited insight gained on the influence of specific design parameters and constraints.

In this work, in order to characterize the tradeoff between the power-to-weight ratio versus efficiency, also known as γ-η Pareto front, of the AWT generators, different machine topologies are modeled analytically. Using analytical models, the whole design space can be evaluated in a computationally efficient manner, without the need for a complicated optimization routine. Furthermore, analyzing the whole design space yields data which can be used for sensitivity analysis, i.e. to evaluate the effect of any design parameter on the performance.

Section II describes the specifications required for the AWT generators and the design approach. Section III summarizes the electro-magnetic machine models. Section IV details the thermal models used to identify thermally infeasible designs. Section V summarizes the models estimating the required structural mass. Section VI details the investigated direct search grid. The direct search results are compared and discussed in Section VII. At last the results are verified with FEM in Section VIII. Section IX concludes and gives an outlook on future work.

II. Specifications and Design Strategy

Table I lists the expected operating points of the AWT generators, where the operating points 1–3 occur equally distributed over the power generation time and normal hover, i.e. motor operation occurs during the launch and landing sequences. In case of a fault condition in one of the system components inhibiting the use of a machine pair, the AWT should still safely land for maintenance, resulting in operating points 5–6. Because the majority of the operation time is spent generating power, only the operating points 1–3 will be considered for efficiency calculations, while 4–6 are considered as thermal and electro–magnetic constraints, where u_{conv} is the convective air speed behind the propeller.

TABLE I
Operating points of the AWT generator/motors.

#	Name	$\frac{P}{\text{kW}}$	$\frac{T}{\text{Nm}}$	$\frac{n}{\text{r/min}}$	$\frac{u_{\text{conv}}}{\text{m/s}}$
1	generation point 1	8.3	35.3	2251	55
2	generation point 2	12.9	38.5	3200	55
3	generation point 3	12.5	26.5	4507	55
4	hover normal	6.5	19.7	3121	16
5	hover (rotor out)	11.1	28.4	3728	21
6	no load (rotor out)	0	0.0	7010	55

The aim of the analysis is to investigate the limits of the γ–η characteristics of potential machine topologies in order to identify the optimal machine for the given set of specifications.

The system down time due to maintenance is to be minimized for economic reasons, therefore, only direct drive solutions are considered in this work, omitting mechanical gears, which are maintenance intensive. Furthermore, only permanent magnet (PM) machine topologies are considered, as they reach higher efficiencies, while maintaining a high power density in comparison to their separately exited counterparts or induction machines.

This work considers PM radial flux machines (RFM) featuring internal or external rotors, cf. Fig. 2. The rotors employ either radially magnetized SPM or radially and tangentially magnetized SPM creating a segmented Halbach configuration. Although the winding factor is smaller compared to traditional distributed windings, only single and double layer concentrated windings are considered, since the conduction losses and the weight is reduced due to the shorter end windings [8], [9]. As the last distinction within the RFM topologies, stators with and without tooth-tips are considered, as they lead to different winding filling factors, radii and pronouncing of slotting effects.

As double-rotor axial flux machines (AFM) have been proposed for applications with challenging requirements on power density and efficiency, such as flywheel systems, electric vehicles and wind power generation [10], this work also considers a coreless stator AFM, as shown in [10]–[13], cf. Fig. 3. AFMs with distributed and concentrated windings are considered.

The design space of each machine topology is characterized by a set of geometric parameters as shown in Fig. 2 and Fig. 3, as well as the materials employed for the windings, the magnetic core and permanent magnets. Moreover, each machine is analyzed assuming sinusoidal (BLAC) and block–shaped (BLDC) currents, enabling the evaluation of different driving methods.

Once the design space is defined as in Section VI, γ and η are calculated for each combination of the parameters. The evaluation of the electro-magnetic and structural mass models (cf. Section III) yields the total mass, m_{tot}, conduction losses, $P_{\text{cond}}(\theta_{\text{W}})$, and iron losses for RFMs, $P_{\text{Fe}}(f)$, of each machine at a winding temperature of $\theta_{\text{W}} = \theta_{\text{amb}} = 25\,^{\circ}\text{C}$. The winding temperature is then determined iteratively. The iteration evaluates the thermal model (cf. Section IV) and consequently updates the temperature dependent losses, i.e. the inputs to the thermal model. The round trip efficiency is defined as

$$\eta = \frac{1}{3}\sum_{\#=1}^{3} \frac{T_{\#}\frac{2\pi n_{\#}}{60}}{T_{\#}\frac{2\pi n_{\#}}{60} + P_{\text{cond,\#}} + P_{\text{Fe,\#}}}, \tag{1}$$

where $P_{\text{cond,\#}}$, and $P_{\text{Fe,\#}}$ are the losses at the operating points steady state temperatures. The power-to-weight ratio is defined by the maximum output power in Table I:

$$\gamma = T_{\#2}\frac{2\pi n_{\#2}}{60}\frac{1}{m_{\text{tot}}}. \tag{2}$$

III. Electro–Magnetic Machine Models

A. Radial Flux Machines

The geometric models of the considered radial flux machines are shown in Fig. 2. The independent parameters are the pole pair p slot number Q_{s} combinations, p/Q_{s}, the stator radius R_{s}, the magnet height h, the air gap width g, the slot depth d_{s}, the pole and slot coverage factors α_{p} and α_{q}, the stack length L of the machine, and the materials employed.

For a given set of independent parameters the back Electro-Motive-Force (EMF) waveform can be calculated. First the

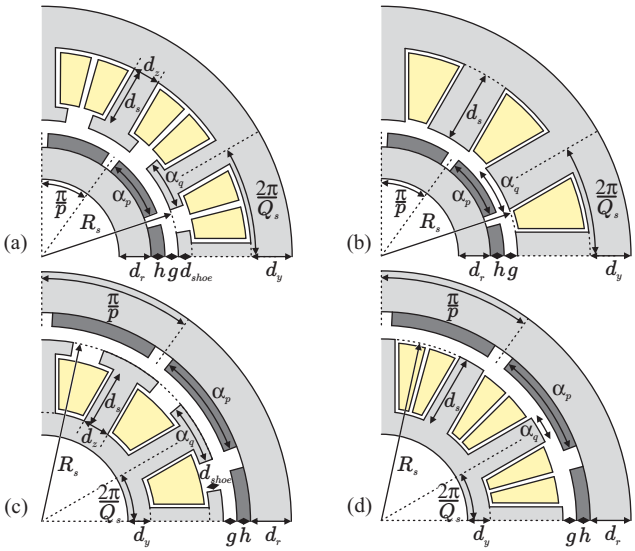

Fig. 2. Geometrical models of the considered radial flux machines, (a) with internal rotor and double layer concentrated windings and stator with tooth–tips, (b) with internal rotor and single layer concentrated windings and stator without tooth–tips, (c) with external rotor and single layer concentrated windings and stator with tooth–tips, (d) with external rotor and double layer concentrated windings and stator without tooth–tips.

open circuit radial air gap field at the stator $B_{\mathrm{r}}(R_{\mathrm{s}}, \alpha, \theta)$, generated by the permanent magnets, is calculated for one electrical rotation of the rotor, i.e. $\theta = \omega t \in [-\frac{\pi}{p}, \frac{\pi}{p}]$, according to [14], [15]. For segmented Halbach magnetization the air gap field $B_{\mathrm{r}}(R_{\mathrm{s}}, \alpha, \theta)$ is calculated according to [16]. The effects of stator slotting $\lambda(R_{\mathrm{s}}, \alpha)$ are included according to [17]. Therefore the flux linkage in phase A is calculated by integration of the radial field seen by the phase coils,

$$\Psi_{\mathrm{ph,A}}(\theta) = L R_{\mathrm{s}} \sum_{k \in \mathrm{ph,A}} \int_{-\alpha_k}^{\alpha_k} B_{\mathrm{r}}(R_{\mathrm{s}}, \alpha, \theta) \cdot \lambda(R_{\mathrm{s}}, \alpha) \mathrm{d}\alpha, \quad (3)$$

with

$$\alpha_k = \frac{\pi}{Q_{\mathrm{s}}} \left(1 + \frac{4(k-1)}{N_{\mathrm{c}}}\right),$$

where N_{c} is 1 for single layer windings and 2 for double layer windings. This way, not only the fundamental component but the complete back EMF waveform $u_{\mathrm{ph,A}} = -\frac{\mathrm{d}}{\mathrm{d}t}\Psi_{\mathrm{ph,A}}$ is captured and the performance of the machine under BLAC or BLDC drive currents can be accurately estimated. Hence the required phase currents to achieve the maximum torque, i.e. operating point #2, is calculated, using the power balance.

The armature reaction field created by the stator current is evaluated using [18] and the effects of flux leakage are taken into account according to [19], [20]. Under the assumption that an ideal inverter adjusts the armature current to be in phase with the back EMF, the resulting flux densities in the stator and rotor iron are calculated. If the flux density in any stator tooth k exceeds the saturation flux density of the soft magnetic material B_{sat} the machine is discarded, i.e. if

$$\frac{\Psi_{k,\mathrm{A,max}}}{B_{\mathrm{sat}}} > \alpha_{\mathrm{q}} \frac{2\pi R_{\mathrm{s}} L}{Q_{\mathrm{s}}}, \quad (4)$$

where $\Psi_{k,\mathrm{A,max}}$ is the maximum flux, as superposition of PM flux and armature flux, in stator tooth k. If the stator teeth have tooth-tips all remaining geometric parameters are

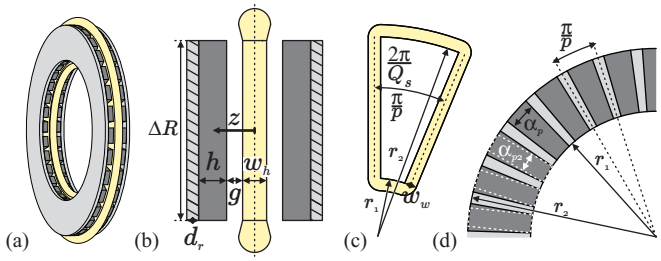

Fig. 3. Geometrical models of the considered axial flux machines (AFM). (a) 3D view of the AFM. The AFM consist of an air cored stator winding and two axially magnetized rotor discs with surface mounted permanent magnets. (b) AFM side cut view. (c) Top view of one coil. (d) Top view of rotor disc.

adjusted, such that the total flux density equals the saturation flux density B_{sat}. This ensures the maximum utilization of the soft magnetic material and defines the winding slot area. The core losses are calculated, neglecting the effect of rotating and non-sinusoidal fields [21],

$$P_{\mathrm{v,Fe}} = V_{\mathrm{s}} \left(k_{\mathrm{h}} f \hat{B}^2 + k_{\mathrm{c}} (f\hat{B})^2 + k_{\mathrm{e}} (f\hat{B})^{1.5}\right), \quad (5)$$

where V_{s} is the stator core volume, f the fundamental electric frequency and $\hat{B}$ is the maximum flux density in the stator core.

Finally, the losses in the conductors are calculated. Because the windings need to be wound on machines with tooth-tips, a winding filling factor of 45% for machines with tooth–tips is assumed. For machines with straight teeth the windings can be wound on coil formers and pressed to increase the filling factor, therefore a higher filling factor of 60% is assumed.

B. Axial Flux Machines

The geometric model of the considered AFM is shown in Fig. 3. The machine consist of two axially magnetized rotor discs, which are either magnetized with SPM on a yoke [10], or SPM in a segmented Halbach configuration as in [12], [22]. The stator in between the rotor discs is an air cored distributed or concentrated winding. The independent parameters are the number of pole pairs p (distributed winding), or pole pair slot number combination p/Q_{s} (double layer concentrated windings), the inner radius r_1 the difference to the outer radius ΔR, the magnet height h, the air gap width g and the winding height w_{h}.

For a given set of independent parameters the open circuit axial field $B_{\mathrm{z}}(r, \phi, z)$ in the air gap is calculated, according to [10] for SPM on a yoke, where the PMs either feature a trapezoidal or rectangular shape. For PMs in a segmented Halbach configuration the open circuit axial field $B_{\mathrm{z}}(r, \phi, z)$ is given in [22]. As the torque per ampere can be obtained by calculating the Lorentz force acting on the windings, the flux linkage can be obtained from the power balance as

$$\Psi_{\mathrm{ph,A}}(\theta) = 4p \int_{0}^{\frac{w_{\mathrm{h}}}{2}} \int_{r_1}^{r_2} \int_{\phi_{\mathrm{s}}}^{\phi_{\mathrm{e}}} r \cdot B_{\mathrm{z}}(r, \phi, z)\ \mathrm{d}\phi\ \mathrm{d}r\ \mathrm{d}z \quad (6)$$

with

$$\phi_{\mathrm{s}} = \tan^{-1}\left(\frac{-w_{\mathrm{w}}}{2r}\right) + \theta \text{ and } \phi_{\mathrm{e}} = \tan^{-1}\left(\frac{w_{\mathrm{w}}}{2r}\right) + \theta\ .$$

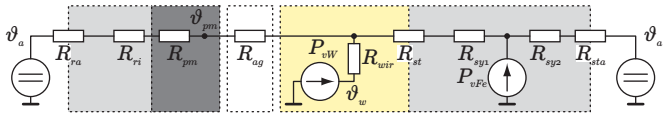

Fig. 4. Simplified radial lumped parameter thermal network (LPTN) of the RFM, the thermal resistances are: R_{ra} convective resistance from rotor yoke to air, R_{ri} conductive resistance through rotor yoke, R_{pm} conductive resistance through PM, R_{ag} convective resistance in the air gap, R_{wir} conductive resistance from winding to stator, R_{st} equivalent conductive resistance through the stator teeth, R_{sy1} first and R_{sy2} second half of conductive resistance through the stator yoke and R_{sta} convective resistance from stator to ambient air. P_{vW} are the conduction losses and P_{vFe} are the core losses.

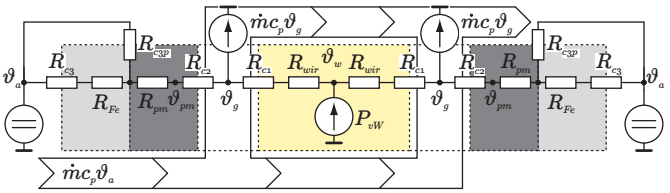

Fig. 5. LPTN of the AFM, the thermal resistances are: R_{c3} convective resistance from rotor disc surface to ambient air, R_{c3p} convective resistance from rotor disc perimeter to ambient air, R_{Fe} conductive resistance through the rotor disc core, R_{pm} conductive resistance through the PM of rotor disc, R_{c1} and R_{c1} convective resistances at the rotor and stator disc surfaces and R_{wir} conductive resistance from the middle of the stator to the stator surface.

With the flux linkage the performance of the machine under BLAC or BLDC drive currents can be accurately estimated analog to section III-A. An important difference between the AFM and the RFM is that the stator core losses are omitted, as the AFM has an air core stator.

IV. Thermal Models

As described in Section III the machines are designed such that they operate on the limits imposed by the electromagnetic components. A second modeling step describes the machine's thermal behaviour, which in return influences important temperature dependent material properties, such as electric conductivity, and therefore influences the torque and losses of the machine. Boglietti [23] outlined the qualities and limitations of different modeling approaches, i.e. finite element modeling (FEM), computational fluid dynamics (CFD) and lumped parameter thermal networks (LPTN). As low computational effort is required simlified LPTN are used [24] to calculate the approximate temperatures of the windings and the permanent magnets.

A. Radial Flux Machines

The simplified LPTN for the RFM is shown in Fig. 4. The thermal resistance from the winding to the stator teeth (and yoke) is approximated as:

$$R_{\mathrm{wir}} = \frac{1}{Q_{\mathrm{s}} L}\left(\frac{t_{\mathrm{iso}}}{k_{\mathrm{iso}} l_{\mathrm{slot}}}\right) \tag{7}$$

with insulation thickness $t_{\mathrm{iso}} = 0.2\,\mathrm{mm}$, insulation conductivity $k_{\mathrm{iso}} = 0.2\,\mathrm{W/mK}$ and slot perimeter l_{slot}.

The remaining conductive thermal resistances are approximated as hollow cylinders [24],

$$R_{\mathrm{th,cond}} = \frac{1}{2\pi k L}\ln\left(\frac{R_{\mathrm{out}}}{R_{\mathrm{in}}}\right), \tag{8}$$

where R_{out} is the outer, R_{in} the inner radius of the hollow cylinder and k the materials thermal conductivity, cf. Table II. This defines the radial thermal resistance of the rotor yoke R_{ri}, the permanent magnets R_{pm} and first R_{sy1} and second R_{sy2} half of the stator yoke. For the thermal resistance of the stator teeth to rotor yoke R_{st}, the thermal resistance is diminished by the percentage of stator teeth volume to stator teeth and slot volume

$$\approx \frac{d_z d_s}{\frac{\pi}{Q_s}\left[\pm(R_s \pm d_{\mathrm{shoe}} \pm d_s)^2 \mp (R_s \pm d_{\mathrm{shoe}})^2\right]}. \tag{9}$$

The convective thermal resistances are expressed as

$$R_{\mathrm{th,conv}} = \frac{1}{A_{\mathrm{c}} h_{\mathrm{c}}} \tag{10}$$

with the convective surface area A_{c} and the average heat transfer coefficient h_{c}.

For the air gap thermal resistance the model given in [26] is employed. The convective surface area is $\mathrm{A_{c,ag}} = 2\pi R_{\mathrm{m}} L$ where R_{m} is the radius of the PM surface and the air gap average heat transfer coefficient is given as

$$h_{\mathrm{c,ag}} = \frac{k_{\mathrm{air}}}{2g}\cdot 0.03\left(\frac{2g\omega R_{\mathrm{m}}}{\nu_{\mathrm{air}}}\right)^{0.8}, \tag{11}$$

with the rotors angular velocity ω, the thermal conductivity k_{air} and viscosity ν_{air} of air.

At last, a heat transfer coefficient of $h_{\mathrm{c,sta}} = 750\,\mathrm{W/m^2K}$ for the stator surface and $h_{\mathrm{c,ra}} = 250\,\mathrm{W/m^2K}$ for the rotor surface is assumed, based on [3]. No axial heat transfer is considered.

B. Axial Flux Machines

The LPTN for the AFM is shown in Fig. 5. The thermal resistance from the stator center to the stator surface is approximated with the thermal resistance in axial direction for a uniform loss distribution

$$R_{\mathrm{wir}} = \frac{1}{8\pi k_{\mathrm{eq}}}\frac{w_{\mathrm{h}}}{\Delta R^2 + 2\Delta R r_1}, \tag{12}$$

where k_{eq} is the mean thermal conductivity of the stator winding conductor and epoxy mixture. The other conductive thermal resistances are calculated with the materials thermal conductivity k, cf. Table II. With the disc surface area $A_{\mathrm{disc}} = \pi(r_2^2 - r_1^2)$, the conductive thermal resistances are

$$R_{\mathrm{pm}} = \frac{h}{A_{\mathrm{disc}}\, k_{\mathrm{pm}}} \text{ and } R_{\mathrm{Fe}} = \frac{d_{\mathrm{r}}}{A_{\mathrm{disc}}\, k_{\mathrm{Fe}}}. \tag{13}$$

The convective thermal resistances are expressed as in (10). With the convective surface areas of the disc, A_{disc}, and perimeter area $A_{\mathrm{perim}} = 2\pi r_2(d_{\mathrm{r}} + h)$, the heat transfer coefficients may be calculated as in [25], [26].

The heat transfer coefficient at the stator to air gap boundary is

$$\overline{h}_{\mathrm{c1}} = \frac{k_{\mathrm{air}}\overline{\mathrm{Nu}}_{\mathrm{c1}}}{R} \text{ with } \overline{\mathrm{Nu}}_{\mathrm{c1}} = 0.333\,\frac{\dot{V}/2}{\pi\nu_{\mathrm{air}} R} \tag{14}$$

where $R = \frac{r_1+r_2}{2}$ is the mean radius. It is assumed that the same heat transfer coefficient in the air gap can be used for the stator air and rotor air boundary, $\overline{h}_{\mathrm{c1}} = \overline{h}_{\mathrm{c2}}$.

For the heat transfer coefficient of the outside surface to the outside air, $\overline{h}_{\mathrm{c3}}$, the (tangential) Reynolds number,

$$\mathrm{Re}_{\varphi}(R) = \frac{\omega R^2}{\nu_{\mathrm{air}}}, \tag{15}$$

is used to asses the flow structure, where ω is the discs rotational speed. If $\mathrm{Re}_\varphi < 2.8 \cdot 10^5$ the laminar flow heat transfer coefficient,

$$\overline{h}_{\mathrm{c3}}^{\mathrm{lam}} \approx 0.35\ k_{\mathrm{air}} \sqrt{\frac{\omega}{\nu_{air}}}, \tag{16}$$

is used. If $\mathrm{Re}_\varphi(R) > 2.8 \cdot 10^5$, the turbulent flow heat transfer coefficient,

$$\overline{h}_{\mathrm{c3}}^{\mathrm{turb}} = \frac{\mathrm{Nu}_{\mathrm{c3}} k_{\mathrm{air}}}{R} \text{ with } \mathrm{Nu}_{\mathrm{c3}} = 0.0151\ \mathrm{Re}_\varphi^{0.8}, \tag{17}$$

is used. The heat transfer coefficient for the rotor radial peripheral edge is,

$$\overline{h}_{\mathrm{c3p}} = \frac{k_{\mathrm{air}} \mathrm{Nu}_{\mathrm{c3p}}}{2\ r_2} \text{ with } \mathrm{Nu}_{\mathrm{c3p}} = 0.133\ \mathrm{Re}_{\mathrm{c3p}}^{\frac{2}{3}} \mathrm{Pr}^{\frac{1}{3}}, \tag{18}$$

where Pr is the Prandtl number for air and the peripheral Reynolds number is

$$\mathrm{Re}_{\mathrm{c3p}} = \frac{\omega (2 r_2)^2}{\nu_{\mathrm{air}}}. \tag{19}$$

A volumetric flow rate $\dot{V} = \dot{m}/\rho$ of the air flowing radially across the stator and rotor magnet surfaces is assumed to be $\dot{V} = 7\,\mathrm{dm}^3/\mathrm{s}$, which is a conservative estimate calculated based on the inner radius r_1 and the convective air speed u_{conv}, and could be enforced by a small axial fan.

V. Structural Mass

As the weight of the electro-magnetic material is minimized, the contributions of the electromagnetic inactive material, such as bearings and housings, to the total machine weight, m_{tot}, becomes more pronounced. In order to choose the right machine, the weight of those components is estimated. The structural mass models use a list of 27 ball bearings, which can operate at the maximum rotational speed of $7010\,\mathrm{r/min}$. The list provides discrete values for the bearings mass, and the bearings inner and outer radii. For each machine the bearing, which results in minimal structural mass, is selected.

A. Radial Flux Machines

Fig. 6 shows the model to estimate the structural mass of an internal rotor RFM. The bearings, magnets and rotor core are mounted on a $3\,\mathrm{mm}$ thick hollow aluminum shaft. The bearing outside radius is limited to $r_{\mathrm{out}} \leq R_{\mathrm{s}} - 3\,\mathrm{mm}$, and the inside radius is limited to $r_{\mathrm{in}} \leq R_{\mathrm{s}} - g - h - d_{\mathrm{r}}$. In order to avoid collisions between the end windings and the respective parts, the end winding height is estimated from the stator geometry and a clearance of $1.5\,\mathrm{mm}$ is added. The bearing shields are approximated as $2\,\mathrm{mm}$ thick discs, which connect to the $3\,\mathrm{mm}$ thick housing with cooling fins. In order to guarantee the cooling properties assumed in Section IV-A, the RFMs feature aluminum cooling fins, which have a thickness of $1\,\mathrm{mm}$, a height of $12\,\mathrm{mm}$, and have a spacing of $3.5\,\mathrm{mm}$ in between.

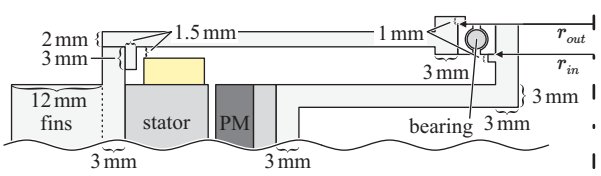

Fig. 6. Sectional drawing of an internal rotor machine including the electromagnetically inactive materials. The magnets and rotor core are mounted on a $3\,\mathrm{mm}$ thick hollow shaft. The stator housing features cooling fins, which have a thickness of $1\,\mathrm{mm}$, a hight of $12\,\mathrm{mm}$, and a spacing of $3.5\,\mathrm{mm}$ in between. The bearing shields are approximated as $2\,\mathrm{mm}$ thick discs.

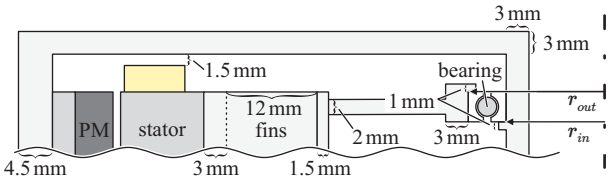

Fig. 7. Sectional drawing of an external rotor machine including electromagnetically inactive materials. The stator is mounted on a $3\,\mathrm{mm}$ thick housing with cooling fins, which have a thickness of $1\,\mathrm{mm}$, a hight of $12\,\mathrm{mm}$, and a spacing of $3.5\,\mathrm{mm}$ in between. A bearing sleeve connects the housing and bearings. The shaft extends, on one side, around the stator to hold the magnets and the rotor core.

Fig. 7 shows the model to estimate the structural mass of an external rotor RFM. The stator is mounted on a $3\,\mathrm{mm}$ thick housing with the same cooling fin structure as an internal rotor RFM, which then connect to a bearing sleeve and the bearings. The bearing outside radius is limited to $r_{\mathrm{out}} \leq R_{\mathrm{s}} - d_{\mathrm{shoe}} - d_{\mathrm{s}} - d_{\mathrm{y}} - 18\,\mathrm{mm}$. The shaft extends around the stator on one side and holds the magnets and rotor core. The added clearance between the end windings and the shaft is also $1.5\,\mathrm{mm}$.

B. Axial Flux Machines

Fig. 8 shows the model to estimate the structural mass of an AFM. The stator winding is fixed in place with a glass-/carbon-fiber reinforced polymer foam core sandwich disc. The disc connects the stator winding to a central static hub. The static hub is a $3\,\mathrm{mm}$ thick hollow cylinder with a $3\,\mathrm{mm}$ thick disc interface. The rotor core and permanent magnets are mounted on $4\,\mathrm{mm}$ thick aluminum discs. The attracting forces from the permanent magnets, which pull the two rotor disc together, are held by the bearings and spacer bolts at the outer rim.

VI. Direct Search Grid

As described in Section II the design space is characterized by the range of free geometric parameters and the considered materials. Table II list the properties of the considered materials. The considered materials are: aluminum and copper windings; neodymium iron boron (NdFeB) magnets, samarium cobalt (SmCo) magnets, and samarium iron nitride bonded (SmFeN) magnets. Although the density of cobalt iron (CoFe) is about $4\,\%$ higher than the density of silicon iron (SiFe), only cobalt iron ($0.1\,\mathrm{mm}$ Vacoflux 48) is considered. In terms

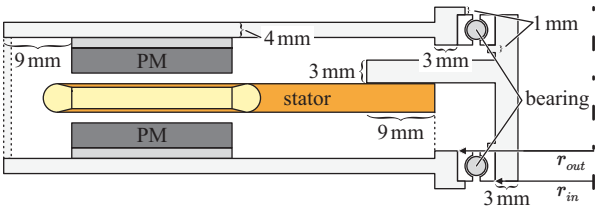

Fig. 8. Sectional drawing of an AFM including the electromagnetically inactive materials. The stator winding GFRP/CFRP foam core sandwich disc is mounted on a central static hub. The rotor core and permanent magnets are mounted on $4\,\mathrm{mm}$ thick aluminum discs, held in place by the bearings and spacer bolts.

of weight reduction a better performance is always achieved with CoFe, because of the higher saturation flux density (2.3 T versus 1.8 T), e.g. for the same flux the thickness of a stator tooth can be reduced by at least 25 % with CoFe. The core loss coefficients k_h, k_c, and k_e in (5), were fitted to experimental lab data of 0.1 mm Vacoflux 48, provided by Vacuumschmelze.

TABLE II
MATERIAL PROPERTIES

material	electric resistivity Ωm	thermal conductivity W/mK	relative permeability	rem. flux density T	mass density kg/m^3
Cu	1.72E^{-8}	350	1	0	8940
Al	2.78E^{-8}	210	1	0	2700
SiFe	5.00E^{-7}	30	∞	0	7800
CoFe	8.50E^{-7}	30	∞	0	8120
NdFeB	1.60E^{-6}	8	1.05	1.25	7800
SmCo	6.75E^{-7}	10	1.03	1.05	8300
SmFeN	1.00E^{4}	1	1.10	0.7	4800

The RFMs considered in this paper feature the pole pair slot number combinations: $\frac{p}{Q_\mathrm{s}} = \{\frac{20}{42}, \frac{20}{48}, \frac{21}{36}, \frac{22}{42}, \frac{23}{48}, \frac{24}{54}, \frac{25}{48}, \frac{25}{60}, \frac{26}{54}, \frac{28}{54}, \frac{28}{48}, \frac{29}{60}, \frac{30}{72}\}$. The stack length L ranges from 15 mm to 75 mm with a step size of 2.5 mm. The slot depth d_s ranges from 5 mm to 25 mm with a step size of 5 mm. The stator radius R_s ranges from 35 mm to 95 mm, for internal rotor machines, and from 45 mm to 105 mm, for external rotor machines, where the step size is 7.5 mm for internal rotor and external rotor machines. The magnet height h ranges from 2 mm to 8 mm with a step size of 2 mm. For Halbach magnetized rotors the pole coverage factor is $\alpha_\mathrm{p} = 100\,\%$, otherwise α_p ranges from 60 % to 100 % with a step size of 10 %. The slot coverage factor α_q ranges from 60 % to 85 % with a step size of 6.25 % for designs with tooth-tips, and from 40 % to 65 % with a step size of 5 %, for designs without tooth-tips. The air gap width g is set to 1 mm.

The AFMs with distributed windings consider the same pole pair numbers as the RFM. The AFMs with concentrated windings consider the same pole pair slot number combinations as the RFMs, but only double layer windings are considered. The inside radius r_1 ranges from 60 mm to 110 mm with a step size of 10 mm. The difference to the outer radius ΔR ranges from 10 mm to 60 mm with a step size of 10 mm. The magnet height h and winding height w_h range from 2 mm to 7 mm with step sizes of 1 mm. For Halbach magnetized rotors the pole coverage factor is $\alpha_\mathrm{p} = 100\,\%$, otherwise α_p ranges from 60 % to 100 % with a step size of 10 %. In order to avoid collisions of the end windings, the winding width is expressed as a function of r_1 and yields

$$w_\mathrm{w}^\mathrm{dist} = w_\mathrm{frac}\ 2\ r_1 \sin\left(\frac{\pi}{3p}\right), \tag{20}$$

for distributed windings and

$$w_\mathrm{w}^\mathrm{conc} = w_\mathrm{frac}\ 2\ r_1 \sin\left(\frac{\pi}{Q_\mathrm{s}}\right), \tag{21}$$

for concentrated windings, where w_frac ranges from 45 % to 85 % with s a step size of 10 %. The air gap width g is set to 1 mm.

VII. Optimization Results

Fig. 9 shows the winding temperatures of the swept internal rotor Halbach RFM in the γ-η Plane. Thermally infeasible designs, i.e. winding temperatures $\theta_\mathrm{W} > 125\,^\circ\mathrm{C}$ or permanent magnet temperatures $\theta_\mathrm{PM} > 90\,^\circ\mathrm{C}$, are colored black. The Pareto fronts neglecting the thermally dependent losses are superimposed to visualize the loss of efficiency caused by the increased winding temperature. Fig. 10 shows the winding temperatures of the swept AFM Halbach with distributed windings. For both RFM and AFM, the highest achievable power-to-weight ratios are not defined by electromagnetic limits, but thermal limits. A comparison of Fig. 9 and Fig. 10 revels that an AFM can more easily be forced air cooled. This is because the assumption of a volumetric flow rate of $\dot{V} = 7\,\mathrm{dm}^3/\mathrm{s}$ through the AFM is conservative and could be enforced by a small axial fan, whereas the heat transfer coefficient of $h_\mathrm{c,sta} = 750\,\mathrm{W/m^2K}$ for the RFM stator surface is high due to the high convective air speed of $u_\mathrm{conv} = 55\,\mathrm{m/s}$.

The direct search grid can be checked a posteriori, to ensure that the grid ranges covers the relevant design space. Fig. 11

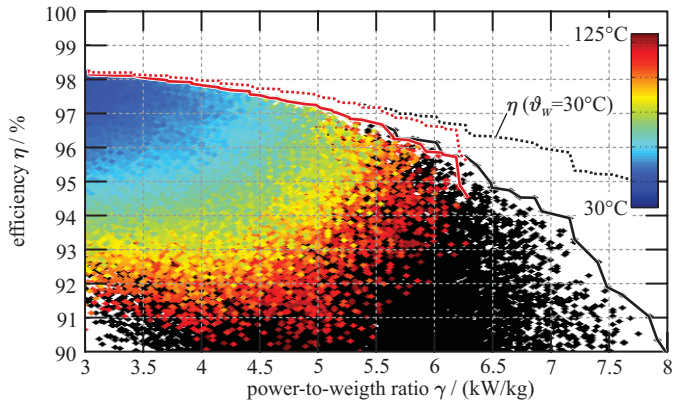

Fig. 9. Winding temperatures of the internal rotor Halbach RFM without tooth-tips, in the power-to-weight ratio versus efficiency plane, i.e. γ-η plane. Machines with winding temperatures $\theta_\mathrm{W} > 125\,^\circ\mathrm{C}$ or permanent magnet temperatures $\theta_\mathrm{PM} > 90\,^\circ\mathrm{C}$, are colored black. The Pareto optimal front, if a winding temperature of only $\theta_\mathrm{W} = 30\,^\circ\mathrm{C}$ is assumed, is superimposed.

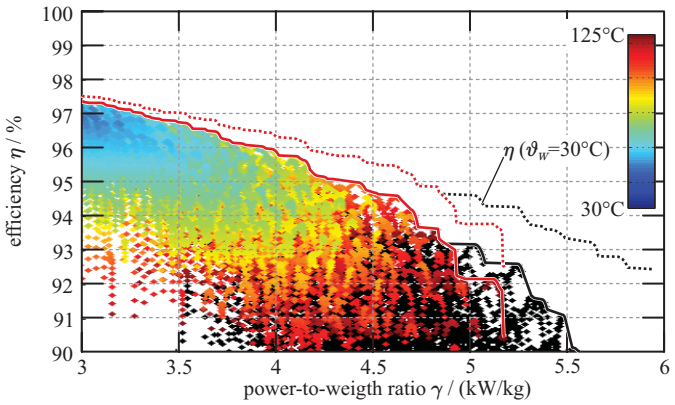

Fig. 10. Winding temperatures of the AFM Halbach with distributed windings, in the power-to-weight ratio versus efficiency plane, i.e. γ-η plane. Machines with winding temperatures $\theta_\mathrm{W} > 125\,^\circ\mathrm{C}$ or permanent magnet temperatures $\theta_\mathrm{PM} > 90\,^\circ\mathrm{C}$, are colored black. The Pareto optimal front, if a winding temperature of only $\theta_\mathrm{W} = 30\,^\circ\mathrm{C}$ is assumed, is superimposed.

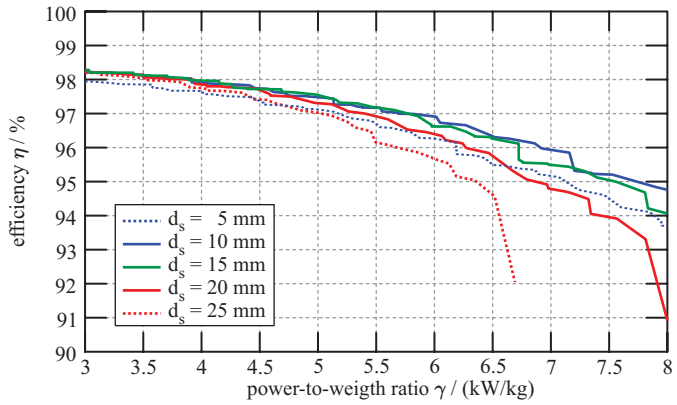

Fig. 11. Pareto fronts of internal rotor Halbach RFM without tooth-tips for each slot depth value, d_s, covered by the grid defined in Section VI.

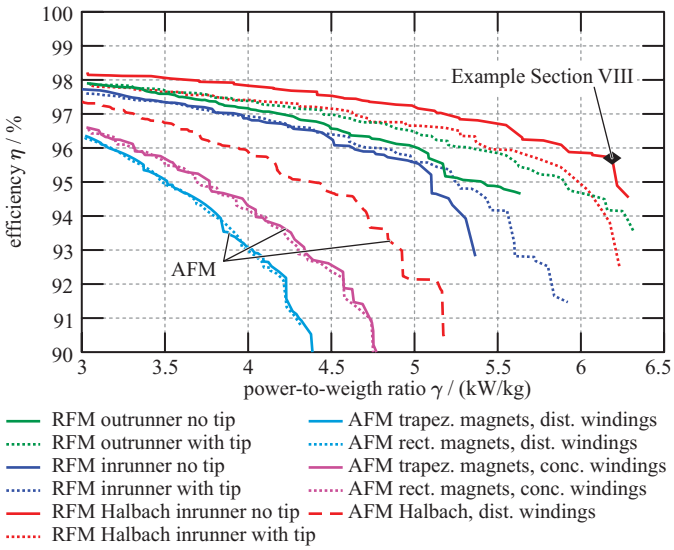

Fig. 12. Power-to-weight ratio versus efficiency γ-η Pareto fronts of all calculated machine topologies, for the parameter ranges described in Section VI. Each design fulfills the specifications listed in Table I and is thermally feasible.

shows the Pareto fronts of solution subsets, for the internal rotor Halbach RFM without tooth-tips. Each solution subsets contains only a single slot depth value, d_s. It can be concluded that the full range of relevant slot depth is covered by the grid, because neither of the subsets at the edges of the grid, i.e. $d_\mathrm{s} = 5\,\mathrm{mm}$ and $d_\mathrm{s} = 25\,\mathrm{mm}$, yield the best performance.

The comparison of Pareto fronts is a useful tool to analyse the sensitivity of any of the grid parameters on the overall performance. It can also be used to compare discrete design choices, which can be summarized as:

- All machine topologies perform best with NdFeB magnets. However, because the eddy current losses in the magnets are neglected, magnet segmentation may be required.
- Double layer windings, perform better than single layer windings, for all RFM topologies. This can be attributed to the shorter length of the end windings.
- For all RFM topologies the use of aluminum windings instead of copper windings yields no change in performance.
- For AFM topologies, the performance is always reduced with aluminum (instead of copper) windings. This can be attributed to the reduction of the back EMF for larger air gaps, e.g. for two AFM which only differ in winding height, w_h, such that the winding resistances of an aluminum and a copper winding are equal, the air gap of the aluminum winding AFM will be larger.

Because the γ-η Pareto fronts provides a criterion to characterize the tradeoff between system efficiency and the required weight, the interaction with the motor inverter should also be considered. This is particularly important for the air cored AFMs, as they exhibit low phase inductances and may lead to a high current ripple, which in turn reduces the efficiency. This effect can be compensated with an increase of the switching frequency of the inverter, i.e. a direct tradeoff of the loss distribution between the motor and the inverter exist. Therefore the complete system, i.e. the motor with the inverter, should be considered for final representation in the γ-η plane. However, if the inverter losses are neglected, all topologies are more efficient when driven with BLAC, rather than BLDC.

Fig. 12 shows the γ-η Pareto fronts for all calculated machine topologies. The Pareto fronts include the temperature dependent losses. From Fig. 12 the following machine topology comparisons may be deduced:

- The performance of the AFM is not sensitive to the use of rectangular magnets, instead of trapezoidal magnets, which can be attributed to the high number of pole pairs.
- AFM with concentrated windings yield a better performance as the AFM with distributed windings, which can be attributed to the shorter end windings and a higher filling factor of 0.7 versus 0.55.
- Halbach magnetized rotors significantly increase the performance for RFM and AFM topologies, which can be attributed to the higher air gap flux density achieved with the Halbach magnetization and lower rotor weight.
- The external rotor RFM designs perform better than the internal rotor designs.
- Any RFM design should feature an efficiency above $\eta \approx 95\,\%$, in spite of the high external heat transfer coefficient, $h_\mathrm{c,sta} = 750\,\mathrm{W/m^2K}$, assumed at the stator surface.

The highest achievable power-to-weight ratio for the specifications given in Table I is $\gamma \approx 6.3\,\mathrm{kW/kg}$, considering only thermally feasible designs and including the structural mass ($\approx 33\,\%$). The Pareto optimal machine topology in this case is an internal rotor Halbach RFM with straight teeth.

VIII. Result Verification

Each analytical model was found to be in accordance with FEM simulations. An example machine is the internal rotor Halbach RFM near the Pareto front with $\gamma \approx 6.2\,\mathrm{kW/kg}$ and $\eta \approx 96\,\%$. The example machine parameters are $p/Q_\mathrm{s} = 25/60$, $R_\mathrm{s} = 60\,\mathrm{mm}$, $L = 26.25\,\mathrm{mm}$, $d_\mathrm{s} = 10\,\mathrm{mm}$, $h = 6\,\mathrm{mm}$, $g = 1\,\mathrm{mm}$, $\alpha_\mathrm{q} = 37.5\,\%$, $d_\mathrm{z} = 2.36\,\mathrm{mm}$, $d_\mathrm{y} = 1.6\,\mathrm{mm}$, and $d_\mathrm{r} = 0\,\mathrm{mm}$, i.e. air cored rotor. The machine weighs $2.092\,\mathrm{kg}$ of which only $1.387\,\mathrm{kg}$ are from electromagnetically active parts.

Fig. 13 shows a FEM simulation (ANSYS Maxwell) of the example machine, where the core's B-H curve is assumed to be linear with a relative permeability $\mu_\mathrm{r} = 400000$, to

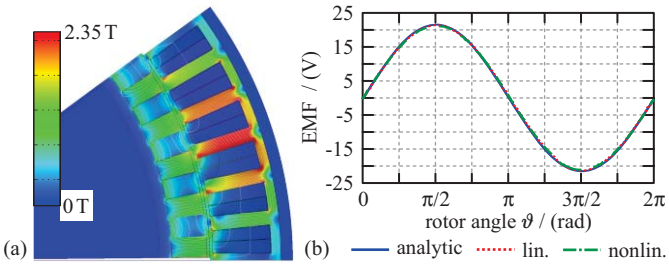

Fig. 13. (a) FEM simulation with linear permeability $\mu_r = 400000$, at the load condition #3 the maximum flux density is 2.3 T. (b) single winding back EMF waveform calculated with the analytical model, linear FEM and nonlinear FEM. The machine is an internal rotor Halbach RFM with parameters: $p/Q_s = 25/60$; $R_s = 60\,\text{mm}$; $L = 26.25\,\text{mm}$; $d_s = 10\,\text{mm}$; $h = 6\,\text{mm}$; $g = 1\,\text{mm}$; $\alpha_q = 37.5\,\%$; $d_z = 2.36\,\text{mm}$; $d_y = 1.6\,\text{mm}$; $d_r = 0\,\text{mm}$.

directly verify the linear analytic models where $\mu_r = \infty$. The maximum flux density at the load condition #2 is $\approx 2.3\,\text{T}$. As the analytical model enforces a maximum flux density of 2.3 T the analytical results are in accordance with the (linear) FEM simulation. The results were also compared to FEM simulations with the CoFe's nonlinear B-H curve. Fig. 13 shows the back EMF waveform of the three models, the deviations from the analytical result are $-0.43\,\%$ with the linear FEM and $-1.16\,\%$ with the nonlinear FEM. The results are summarized in Table III.

TABLE III
RESULTS FOR THE EXAMPLE MACHINE AT $3200\,\text{r/min}$ AND $I_{RMS} = 280\,\text{A}$

calculation method	Torque T/Nm	winding losses P_{cond}/W	core losses P_{Fe}/W	eddy current losses /W
Analytic	38.5	434	63.3	N/A
linear FEM	37.8	N/A	N/A	43.3
(deviation)	1.7 %	—	—	—
nonlin. FEM	36.7	N/A	57.2	43.3
(deviation)	4.6 %	—	9.6 %	—

IX. Conclusion and Outlook

This paper presents the optimization of an electric machine required for an Airborne Wind Turbine. The tradeoff between the power to weight ratio versus efficiency, γ-η Pareto fronts, of different machine topologies are derived and compared. The derivation uses analytical models, which enables the analysis of the whole design space in a computationally efficient manner. The performance of various RFM and AFM topologies are compared and suggest that an internal rotor Halbach RFM without tooth-tips exhibits the best performance for the given specifications. However, two further machine topologies, the external rotor Halbach RFM and the Halbach AFM with concentrated windings, should be added to the analysis. The analytical results are compared to linear and nonlinear FEM simulations and verify the validity of the analytical optimization approach. An example machine reaches a power-to-weight ratio of $\gamma \approx 6.2\,\text{kW/kg}$ ($2.8\,\text{kW/lb}$) at an efficiency of $\eta \approx 96\,\%$. No machine designs with comparable performance have been found in literature or are available in industry.

References

[1] J. W. Kolar, T. Friedli, F. Krismer, A. Looser, M. Schweizer, P. Steimer, and J. Bevirt, "Conceptualization and multi-objective optimization of the electric system of an airborne wind turbine," Proc. of the 20th IEEE International Symposium on Industrial Electronics (ISIE 2011), Gdansk, Poland, 27–30 June 2011, pp. 32–55.

[2] R. A. Friedemann, F. Krismer, J. W. Kolar, "Design of a minimum weight dual active bridge converter for an airborne wind turbine system," Proc. of the 27th Applied Power Electronics Conference and Exposition (APEC 2012), Orlando, Florida, USA, 5–9 Feb. 2012, pp. 509–516.

[3] C. Gammeter, F. Krismer, J. W. Kolar, "Weight optimization of a cooling system composed of fan and extruded fin heat sink," Proc. of the IEEE Energy Conversion Congress and Exposition (ECCE 2013), Denver, Colorado, USA, 15–19 Sept. 2013.

[4] P. Ragot, M. Markovic, Y. Perriard, "Optimization of electric motor for a solar airplane application," IEEE Transactions on Industry Applications, vol. 42, no. 4, pp. 1053–1061, July/Aug. 2006.

[5] Y. Perriard, P. Ragot, M. Markovic. "Brushless dc motor optimization process - choice between standard or straight tooth shape." Proc. of 41th IEEE Industry Applications Society Annual Meeting, Tampa, USA, 8–12 Oct. 2006.

[6] P. Ragot, P. Germano, M. Markovic, Y. Perriard, "Brushless DC motor for a solar airplane application: comparison between simulations and measurements," Proc. of the IEEE Industry Applications Society Annual Meeting, Edmonton, Canada, 8–12 Oct. 2008.

[7] M. Van der Geest, et al. "Optimization and comparison of electrical machines using particle swarm optimization," Proc. of the XXth IEEE International Conference on Electrical Machines (ICEM 2012), Marseille, France, 2–5 Sept. 2012.

[8] M. Van der Geest, et al. "Machine selection and initial design of an aerospace starter/generator." Proc. of the IEEE International Electric Machines and Drives Conference (IEMDC 2013), 12–15 May 2013.

[9] J. Cros and P. Viarouge, "Synthesis of high performance PM motors with concentrated windings," IEEE Transactions on Energy Conversion, vol. 17, no. 2, pp. 248–253, Jun. 2002.

[10] Y. Huang, et al. "3-D analytical modeling of no-load magnetic field of ironless axial flux permanent magnet machine." IEEE Transactions on Magnetics, vol. 48, no.11, pp. 2929-2932, 2012.

[11] O. Winter, C. Kral, E. Schmidt, "Design and loss assessment of air cored axial flux permanent magnet machines." Proc. of the IEEE International Electric Machines and Drives Conference(IEMDC 2013), 12–15 May 2013-

[12] LaunchPoint, Accessed: Februar 2014, [Online], Available: http://www.launchpnt.com/

[13] Flytec, Accessed: Februar 2014, [Online], Available: http://www.flytec.ch/

[14] Zhu, Z. Q., et al. "Instantaneous magnetic field distribution in brushless permanent magnet DC motors. I. Open-circuit field." IEEE Transactions on Magnetics, vol. 29, no. 1. pp. 124–135, 1993.

[15] Z. Q. Zhu, D. Howe, C. C. Chan, "Improved analytical model for predicting the magnetic field distribution in brushless permanent-magnet machines." IEEE Transactions on Magnetics, vol. 38, no. 1, pp. 229-238, 2002.

[16] Y. Shen, G. Y. Liu, Z. P. Xia, Z. Q. Zhu, "Determination of maximum electromagnetic torque in PM brushless machines having two-segment Halbach array," IEEE Transaction on Magnetics, vol. 61, no. 2, pp. 718–729, Feb. 2014.

[17] Z. Q. Zhu, D. Howe. "Instantaneous magnetic field distribution in brushless permanent magnet DC motors. III. Effect of stator slotting." IEEE Transactions on Magnetics, vol. 29, no. 1, pp. 143–151, 1993.

[18] Z. Q. Zhu, D. Howe. "Instantaneous magnetic field distribution in brushless permanent magnet DC motors. II. Armature-reaction field." IEEE Transactions on Magnetics, vol. 29, no. 1, pp. 136-142, 1993.

[19] J. Pyrhönen, T. Jokinen, V. Hrabovcová, "Design of rotating electrical machines," John Wiley and Sons, Ltd, 2008.

[20] J. Mühlethaler. "Modeling and multi-objective optimization of inductive power components," PhD thesis Nr. 20217, ETH Zurich, 2012.

[21] G. Bertotti. "General properties of power losses in soft ferromagnetic materials," IEEE Transactions on Magnetics, vol 24, no. 1, pp. 621–630, 1988.

[22] W. K. Thompson, "Three-dimensional field solutions for multi-pole cylindrical Halbach arrays in an axial orientation," Report, NASA Glenn Research Center, Cleveland, Ohio, 2006.

[23] A. Boglietti, et al. "Evolution and modern approaches for thermal analysis of electrical machines." IEEE Transactions on Industrial Electronics, vol. 56, no. 3, pp. 871–882, 2009.

[24] A. Boglietti, et al. "A simplified thermal model for variable-speed self-cooled industrial induction motor." IEEE Transactions on Industry Applications, vol. 39, no. 4, pp. 945–952, 2003.

[25] J. F. Gieras, R. J. Wang, and M. J. Kamper. "Axial flux permanent magnet brushless machines." 2nd Edition. Springer, 2008.

[26] Howey, David A., Peter RN Childs, and Andrew S. Holmes. "Air-gap convection in rotating electrical machines." IEEE Transactions on Industrial Electronics, vol. 59, no. 3, pp. 1367-1375, 2012.